


In the format provided by the authors and unedited.

A wireless millimetre-scale implantable neural stimulator with ultrasonically powered bidirectional communication

David K. Piech ^{1,2,7}, Benjamin C. Johnson^{3,4,7}, Konlin Shen^{1,2}, M. Meraj Ghanbari ³, Ka Yiu Li³, Ryan M. Neely⁵, Joshua E. Kay³, Jose M. Carmena ^{1,2,3,5} ✉, Michel M. Maharbiz ^{1,2,3,5,6} ✉ and Rikky Muller ^{1,2,3,6} ✉

¹The UC Berkeley–UCSF Graduate Program in Bioengineering, University of California, Berkeley, Berkeley, CA, USA. ²The UC Berkeley–UCSF Graduate Program in Bioengineering, University of California, San Francisco, San Francisco, CA, USA. ³Department of Electrical Engineering and Computer Sciences, University of California, Berkeley, Berkeley, CA, USA. ⁴Department of Electrical Engineering and Computer Engineering, Boise State University, Boise, ID, USA. ⁵Helen Wills Neuroscience Institute, University of California, Berkeley, Berkeley, CA, USA. ⁶Chan Zuckerberg Biohub, San Francisco, CA, USA. ⁷These authors contributed equally: David K. Piech, Benjamin C. Johnson. ✉e-mail: jcarmena@berkeley.edu; maharbiz@berkeley.edu; rikky@berkeley.edu

Contents

Supplementary Section 1: Additional results from characterizing mote performance	2
Figure S1 Backscatter modulation design	2
Figure S2 Further miniaturized StimDust mote	2
Figure S3 External transceiver acoustic field and piezo voltage harvest	3
Table S1: System power performance	5
Supplementary Section 2: Supplementary <i>in vivo</i> results	6
Figure S4 <i>In vivo</i> power harvesting performance during initial power-up	6
Figure S5 Precise control of evoked neural response achieved through varying stimulation current or stimulation pulse duration; second sweep of parameters	7
Figure S6 Supplementary <i>in vivo</i> results: Animals C and F	9
Video S1 <i>In vivo</i> neural stimulation with fully implanted wireless StimDust	9
Supplementary Section 3: Discussion supporting the claim that stimulation was due to the mote output current and was not directly ultrasound-mediated	9
Figure S7 Pilot study: <i>in vivo</i> stimulation and elicitation of compound muscle action potential with electrically-powered mote	10
Supplementary Section 4: Discussion of electrodes and monophasic stimulation	11
Figure S8 Stimulation electrodes characterization in saline	11
Figure S9 Monophasic stimulation and charge balancing	12
Table S2 Charge balance current values from empirically pegged and fit simulations of the stimulation pulse	14
Figure S10 Charge (Q) vs. charge density (Q/A) for safe stimulation limits	15
Figure S11 Charge balance current density vs. square electrode area in saline and <i>in vivo</i>	16
Supplementary Section 5: Additional photographs	16
Figure S12 Alternate images for Fig 1b, Fig 1c, and Fig 1d.	18

Supplementary Section 1: Additional results from characterizing mote performance

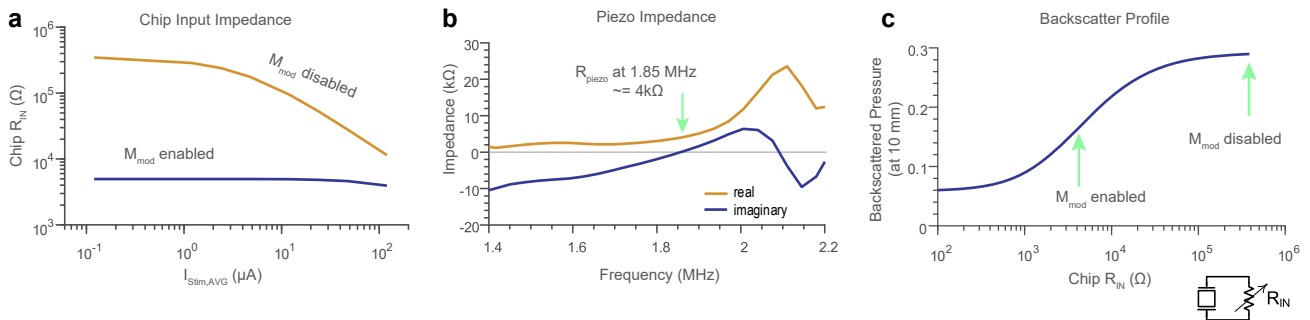


Figure S1 | Backscatter modulation design. **a**, The measured chip input resistance (R_{IN}) for different current stimulation loads. The bottom trace is when the modulation switch is enabled, keeping R_{IN} constant across load. The difference between the two lines is the modulation depth for a given load. **b**, Simulated mote piezo impedance versus frequency. At resonance, the piezo has a $4\text{ k}\Omega$ impedance. **c**, Simulated backscatter profile at 10 mm based for different R_{IN} . $N = 1$ sweep for the data presented in panel (a).

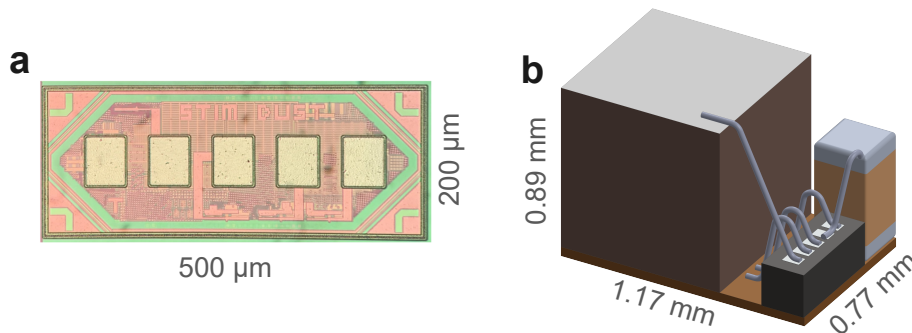


Figure S2 | Further miniaturized StimDust mote. **a**, fabricated further-miniaturized StimDust IC (integrated circuit). **b**, Design of further-miniaturized mote utilizing the fabricated IC and a piezo of the same dimensions as that in Fig 4.

The step response ring-up time of the external transducer was approximately 1 cycle, or $0.56\ \mu\text{s}$. The ring-up time for the external transducer and mote piezo system (full downward link) was approximately 3.5 cycles or $1.94\ \mu\text{s}$. The ring-up time for the external transducer, mote piezo, and backscatter capture system (full bidirectional link) was approximately 4.5 cycles or $2.5\ \mu\text{s}$. A pulse-train mode was demonstrated by interspersing several pulses of short-duration shorting-phase with a pulse of long-duration shorting-phase. This yielded a pulse-train every 500 ms, with each train containing 10 pulses of $100\ \mu\text{s}$ pulse width occurring every $750\ \mu\text{s}$.

The acoustic beam patterns of the 12.7 mm and 25.4 mm diameter external transducers (Supplementary Fig. 3) were had a focal plane intensity transverse full-width-half-maximum of

1.6 mm and 1.8 mm, respectively, and an axial intensity longitudinal full-width-half-maximum of 14 mm and 17.7 mm.

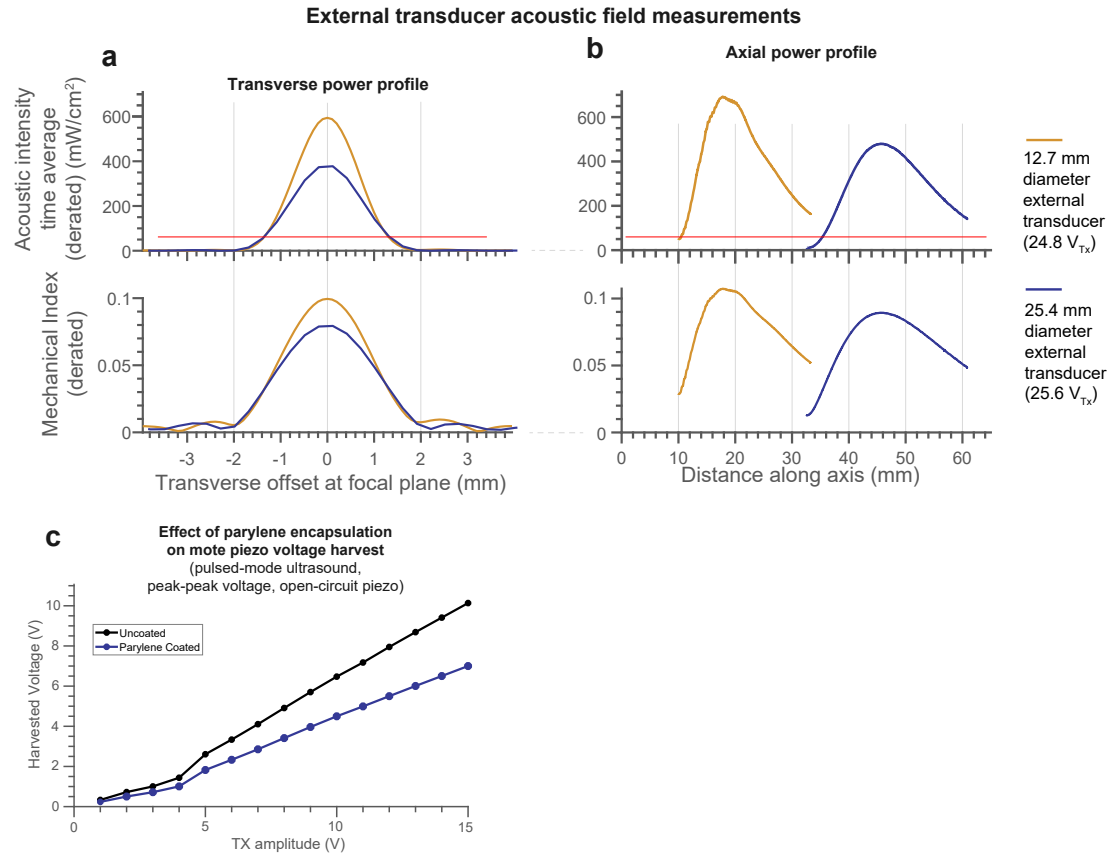


Figure S3 | External transceiver acoustic field and piezo voltage harvest. Characterization of the external transceiver acoustic field for two alternate transducers used for shallow (12.7 mm diameter transducer) and deep operation (25.4 mm diameter transducer). **a**, transverse beampattern. **b**, longitudinal beampattern. Data taken in a water tank with external transceiver and hydrophone. Red lines indicate the minimum acoustic intensity necessary to operate StimDust. **c**, Effect of parylene encapsulation on mote piezo voltage harvest. (a) Shown here is N = 1 fine-stepped sweep of transverse offset; a different coarse-stepped sweep of transverse offset produced similar results. (b) Shown here is N = 1 fine-stepped sweep of axial offset; a different coarse-stepped sweep of axial offset produced similar results. (c) N = 1 voltage sweep for each condition.

The power performance of the system was measured for two conditions: benchtop operation at high PRF (pulse repetition frequency) and *in vivo* operation with a fully implanted mote at low PRF (Supplementary Table 1). V_{TX} and P_{electrical} into the external transducer were measured at the output of the external power supply used to supply the ultrasound interface chip. The external transducer was heavily damped to shorten its impulse response and much of the acoustic power generated in the external transducer piezo was dumped into the absorptive backing layer, causing the electrical input power to acoustic power at the focal plane efficiency to be low.

Acoustic domain measurements were made with a hydrophone in water; notably, the hydrophone measurements were taken in a separate experiment from mote operation and the acoustic values in table 1 assume that the mote was positioned at the point of maximal acoustic intensity (this may cause up to ~20% error). For the *in vivo* condition, the hydrophone measurements could not be made directly, and so expected loss from impedance mismatches and absorption in 2 mm of skin and 3 mm of muscle (¹, ², ³) was modelled to yield an estimate of acoustic intensity inside the animal. The acoustic power at the focal plane (depth of the mote) was integrated over a 1 cm radius circle, which is at least 97% of the total power in the focal plane. The face of the mote captured approximately 20% of the acoustic power in the focal plane. This was a trade-off that balances minimizing the power coupling sensitivity of small transverse misalignments with minimizing the unused ultrasound power radiating into the body.

The acoustic power conversion efficiency (η_{acoustic}) is defined as the ratio of the electrical power used to charge to the mote relative to the acoustic power at the face of the mote piezo. This efficiency encompasses the acoustic to electrical power efficiency of the piezo, the rectifier efficiency, and the standby power consumption of the IC. It was calculated from the measured rate of change of the C_{store} capacitor voltage (V_{DD}) during initial mote power-up for a 3V V_{DD} steady-state. Under a given incident acoustic power, the η_{acoustic} (as measured by P into C_{store}) peaked at ~8.1% when V_{DD} was near half the steady-state voltage (Fig. 6f, Supplementary Fig. 4). The mote's stimulation power ($P_{\text{stimulation_delivered}}$) was calculated by measuring the voltage across an electrode model load. The electrode load was modelled as a solution resistance (R_{soln}) and double-layer capacitance (C_{dl}) in series. R_{soln} and C_{dl} were discrete passives for the benchtop test; *in vivo* values were estimated from the stimulation voltage at known current output by using the initial IR drop (current times resistance voltage drop) and initial slope of capacitive charging. Q_{pulse} (charge per pulse), E_{pulse} , and $P_{\text{stimulation_delivered}}$ were calculated from the measured stimulation voltage waveform, R_{soln} , C_{dl} , and f_{stim} . $P_{\text{stimulation_available}}$ was calculated from Q_{pulse} delivered, the voltage headroom available, and f_{stim} . $P_{\text{stimulation_delivered}}$ represents the power delivered to the electrode model used (and would change with load) while $P_{\text{stimulation_available}}$ represents the maximum stimulation power available for any load.

Note that at low PRF the total $P_{\text{stimulation_delivered}}$ was low and the device charged up quickly and remained 'idle' for most of the time between stimulation pulses yielding a low overall efficiency. Under low PRF conditions, it was shown that the device could be intermittently powered up for each pulse to reduce the overall ultrasound dose. If optimized for this application, the mote could have a small C_{store} to reduce start-up time.

Table S1: System power performance

	Benchtop high PRF example	<i>In vivo</i> low PRF example
Acoustic medium	ultrasound gel	gel, skin, muscle
Mote depth from ext. txdr	48 mm	18 mm
Stimulation protocol		
Specified PRF	2380 Hz	.222 Hz
Specified stim current	400 μ A	400 μ A
Specified stim pulse width	72 μ s	172 μ s
Specified interphase gap	10 μ s	80 μ s
External transceiver		
External transducer	25.4 mm \emptyset	12.7 mm \emptyset
V_{TX}	28.9 V	24.8 V
U/S duty cycle with UFI's	76%	100%
$P_{\text{electrical}}$ drive ext. txdr	2.0 W	1.34 W
I_{SPTA} derated	723 mW/cm ²	713 mW/cm ²
P_{acoustic} at surface over txdr face	20.9 mW	17.7 mW
P_{acoustic} at focal plane in 1 cm radius	20.8 mW	14.6 mW
P_{acoustic} on mote piezo face	4.3 mW	2.8 mW
Mote		
Mote C_{store}	4 μ F	4 μ F
V_{DD} steady state	1.9 V	3.0 V
P into C_{store} average	147 μ W*	9.7 μ W
$\eta_{\text{acoustic_mote_Face} \rightarrow \text{electrical_VDD}}$	3.4%*	0.34%
$\eta_{\text{acoustic_at_surface} \rightarrow \text{electrical_VDD}}$	0.70%	0.06%
Load		
Load R_{soln} (est. for <i>in vivo</i>)	3 k Ω	4.4 k Ω
Load C_{dl} (est. for <i>in vivo</i>)	22 nF	100 nF
Q_{pulse}	24 nC	43.4 nC
E_{pulse}	37 nJ	108 nJ
$P_{\text{stimulation_delivered}}$	89 μ W	24 nW
$P_{\text{stimulation_available}}$	103 μ W	30 nW

* these power values were derived based on the incident acoustic power at the mote face and the measured efficiencies at various V_{DD} s. (' \emptyset ' is diameter; 'UFI' is ultrasound-free interval; 'ext. txdr' is external transducer; 'rad.' is radius; 'soln' is solution.)

Supplementary Section 2: Supplementary *in vivo* results

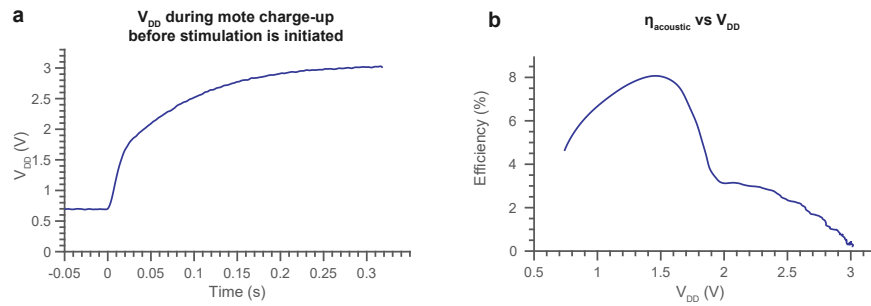


Figure S4 | *In vivo* power harvesting performance during initial power-up. **a**, After 4.2 s without receiving power, the mote V_{DD} (V across C_{store}) was ~ 0.7 V. When downlink power resumed (at $t = 0$), the $4 \mu\text{F}$ C_{store} charged over ~ 300 ms. **b**, The charging waveform from (a) was used to estimate the efficiency during charging as V_{DD} passed through various regimes. $\eta_{acoustic}$ is the ratio of electrical power used for charging the mote to acoustic power at the face of the mote piezo. At $1.2 V_{DD}$, the rate of electrical power harvest was maximum but V_{DD} was below the POR (power-on reset) cut-off and the device did not stimulate. Between $1.9 V_{DD}$ and $3.0 V_{DD}$, the mote was able to stimulate. Power harvest efficiency was moderate at $1.9 V_{DD}$ and decreased to very low values at $3.0 V_{DD}$, which was the point where C_{store} was nearly topped off and ‘trickle charging’ under the given incident acoustic power conditions. Representative example out of $N = 2$ charging periods under this experimental condition.

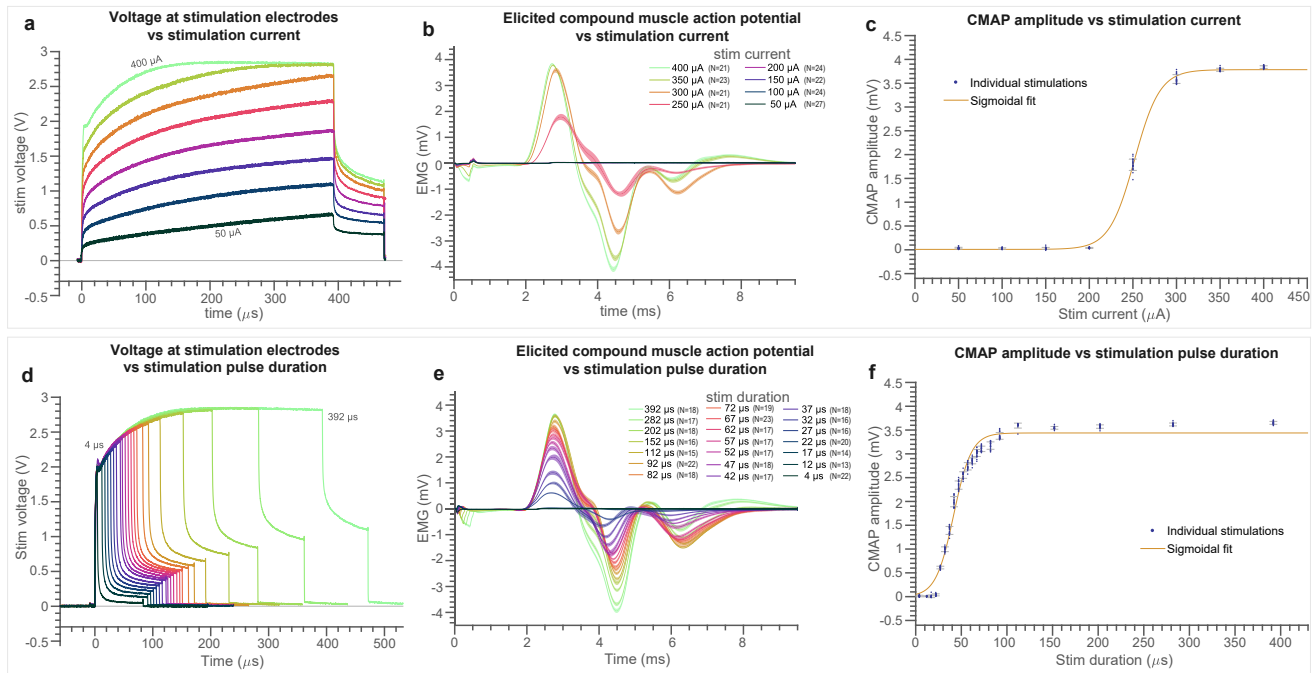
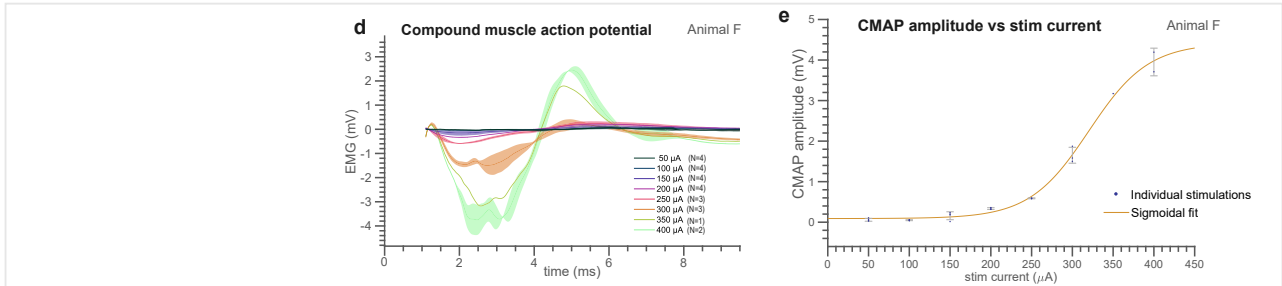
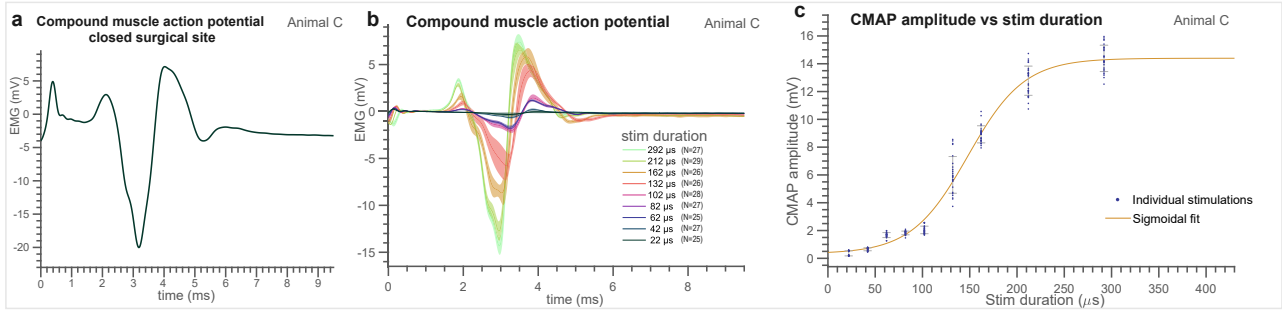


Figure S5 | Precise control of evoked neural response achieved through varying stimulation current or stimulation pulse duration; second sweep of parameters. This data was taken with the same animal and mote as that in Fig. 7, but 2 hours after the first sweep. **[Current-control]:** Stimulation current was varied from 50 μA to 400 μA with stimulation pulse width held at 392 μs . **a**, Stimulation electrode voltage shows an approximately linear trend with stimulation current ($N = 1$ stimulation pulse waveform collected for each condition). **b**, CMAP (compound muscle action potential) waveforms show activation for 250 μA to 400 μA . For each condition, the coloured line represents the trial-average CMAP voltage at each point in time, the width of the shaded error region is ± 1 s.d., and N is the number of pulse events in each condition. The pulse repetition rate of approximately 1/3 Hz yielded essentially independent biological responses to each pulse, though there could have been small non-independent effects due to muscle fatigue. **c**, CMAP amplitude vs. stim current shows a typical sigmoidal recruitment curve. Each point is a single CMAP baseline-to-peak amplitude, the line is a sigmoidal fit and error bars are ± 1 s.d. of the CMAPs in each stim current condition. The sample size for each condition in panel c is the same as that for each condition in panel b. **[Pulse-width-control]:** Stimulation pulse width was varied from 4 μs to 392 μs with stimulation current held at 400 μA . **d**, Stimulation electrode voltage shows an approximately linear trend with stimulation current ($N = 1$ stimulation pulse waveform collected for each condition). **e**, CMAP waveforms show activation from 27 μs to 392 μs . For each condition, the line represents the trial-average CMAP voltage at each point in time, and the width of the shaded error region is ± 1 s.d., and N is the number of pulse events in each condition. This panel shows that the duration of the electrical artefact increased with increasing stimulation pulse width, but the time-course of the CMAP did not appreciably change, with only amplitude differing. **f**, CMAP amplitude vs. stim pulse width shows a typical sigmoidal recruitment curve with little or no evoked response below 27 μs pulse width and saturation at approximately 112 μs pulse width. Each point is a single CMAP baseline-to-peak amplitude, the line is a sigmoidal fit and error bars are ± 1 s.d. of the CMAPs in each stim duration condition. The sample size for each condition in panel f is the same as that for each condition in panel e. Note: This data was taken with an open surgical site. All replications in this figure are separate stimulation events in a single animal.



Muscle co-activation

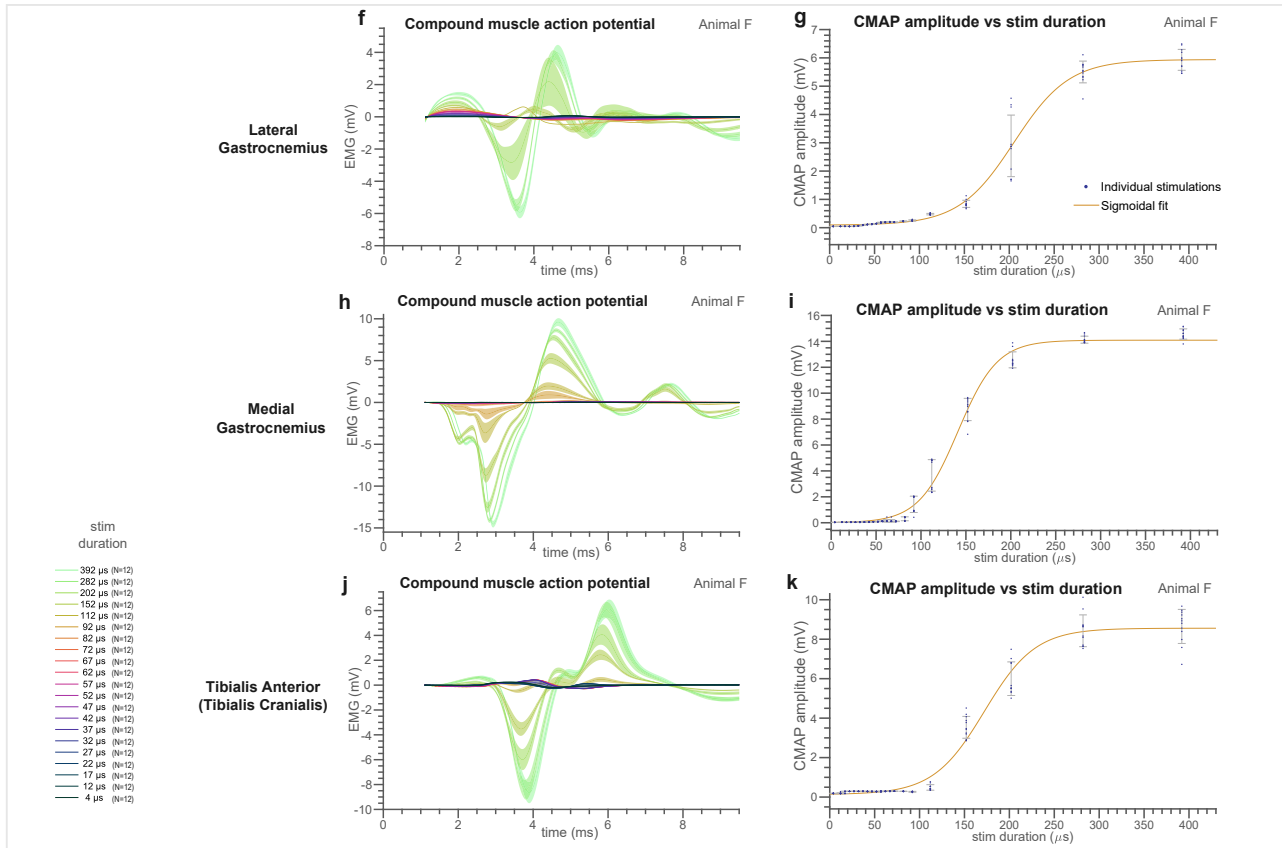


Figure S6 | Supplementary *in vivo* results: Animals C and F. **a**, EMG (electromyogram) trace of CMAP (compound muscle action potential) resulting from stimulation that was performed in Animal C with the ultrasonic link traversing muscle and skin layers between the implantation site and the exterior of the body. Representative example CMAP trace for $N = 1$ stimulation pulse within an experimental condition with 20 stimulation pulses. **b, c**, StimDust operation in animal C at stimulation pulse duration values between $22 \mu\text{s}$ and $292 \mu\text{s}$, with sigmoidal CMAP recruitment. **d, e**, StimDust operation in animal F at stimulation current values between $50 \mu\text{A}$ and $400 \mu\text{A}$, with sigmoidal CMAP recruitment. **f-k**, StimDust operation in animal F at stimulation pulse duration values between $22 \mu\text{s}$ and $392 \mu\text{s}$, with sigmoidal CMAP recruitment across three innervated muscles. In panels **b, d, f, h, and j**, for each condition, the coloured line represents the trial-average CMAP voltage at each point in time, the width of the shaded error region is ± 1 s.d., and N is the number of pulse events in each condition. In panels **c, e, g, i, and k**, each point is a single CMAP baseline-to-peak amplitude, the line is a sigmoidal fit and error bars are ± 1 s.d. of the CMAPs in each stim current condition. The sample size for each condition in panel **c** is the same as that for each condition in panel **b**. The sample size for each condition in panel **e** is the same as that for each condition in panel **d**. The sample size for each condition in panels **f, g, h, i, j, and k** is given on the left-side figure legend. All replications of a given stimulation condition in panels **a-e** are separate stimulation events in animal C. All replications of a given stimulation condition in panels **f-k** are separate stimulation events in animal F. The pulse repetition rate of approximately $1/5$ Hz for all panels in this figure yielded essentially independent biological responses to each pulse, though there could have been small non-independent effects due to muscle fatigue. For animal F (**d-k**), a large stimulation artifact was observed on the EMG traces which interfered with filtering. The stimulation artifact data from 0 ms to 1.125 ms after stimulation onset was not included in the EMG trace analysis and the DC value (zero-value) of the trace was set to the average value between 1.125 ms and 1.25 ms after stimulation onset.

Video S1 | *In vivo* neural stimulation with fully implanted wireless StimDust. Mote implanted on rat sciatic nerve with stimulation pulses delivered at 0.22 Hz. In clips (a) and (b) (animal D), the animal's right hindquarters are visible with cranial to the right and caudal to the left. The closed surgical site is at the centre of the frame and the animal's right leg and foot are towards the bottom left of the frame, with two EMG electrodes visible. The external transducer can be seen at the top of the frame. Ultrasound gel fills the gap between the external transducer and the animal, and a glass slide makes this space visible. Clip (c) shows a view from the rear (animal D). Clip (d) shows a different experiment with the mote implanted on the left sciatic (animal C).

Supplementary Section 3: Discussion supporting the claim that stimulation was due to the mote output current and was not directly ultrasound-mediated

At 1.85 MHz, the threshold of ultrasound-mediated neural stimulation has been reported at approximately 10 W/cm^2 pulse-average intensity⁴; this is more than 14x higher intensity than that used in this study. Furthermore, as the system increased stimulation current from $50 \mu\text{A}$ to $400 \mu\text{A}$ with a corresponding recruitment of CMAP response, acoustic power was nearly identical and actually decreased slightly since the protocol utilizes a longer TDC (time-delay control) gap when specifying high current. Additionally, no EMG response was observed when the system was

driven with continuous ultrasound at the same intensity as used for controlling the device, but with no coded downlink signals. Finally, a pilot *in vivo* experiment, which powered a mote stimulator IC electrically with no ultrasound, produced stimulation and evoked CMAP's similar to those evoked with an acoustically-powered mote (Fig S7). Utilizing a current-control implantable stimulator provides improved stimulation precision and spatial resolution as compared to directly mediated ultrasonic stimulation, and requires substantially lower acoustic intensities and thus has lower risk from ultrasound-induced thermal or cavitation damage⁵.

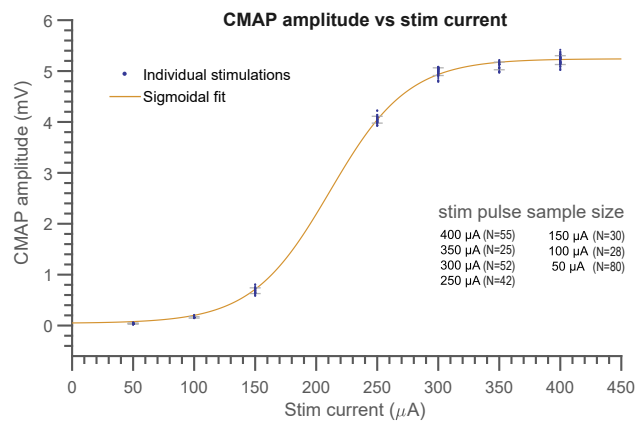


Figure S7 | Pilot study: *in vivo* stimulation and elicitation of compound muscle action potential with electrically-powered mote. A cuff was implanted on the sciatic nerve of a rat. The cuff electrodes were attached to a StimDust mote that was assembled on a larger printed circuit board located outside the animal. The electrical terminals of the external transceiver piezo drive circuit were directly connected to the PZ+ and PZ- terminals of the mote. This entirely bypassed the acoustic wireless link (no ultrasound energy was involved), but otherwise utilized all mote functionality and downlink communication protocol. CMAP amplitude vs. stim current shows a typical sigmoidal recruitment curve which is similar to that measured when utilizing the ultrasound wireless link. Each point is a single CMAP baseline-to-peak amplitude, the line is a sigmoidal fit and error bars are ± 1 s.d. of the CMAPs in each stim current condition. N is the number of pulse events in each condition. The pulse repetition rate of approximately 1 Hz yielded essentially independent biological responses to each pulse, though there could have been small non-independent effects due to muscle fatigue. Note: This data was taken with an open surgical site. All replications in this figure are separate stimulation events in a single animal.

Supplementary Section 4: Discussion of electrodes and monophasic stimulation

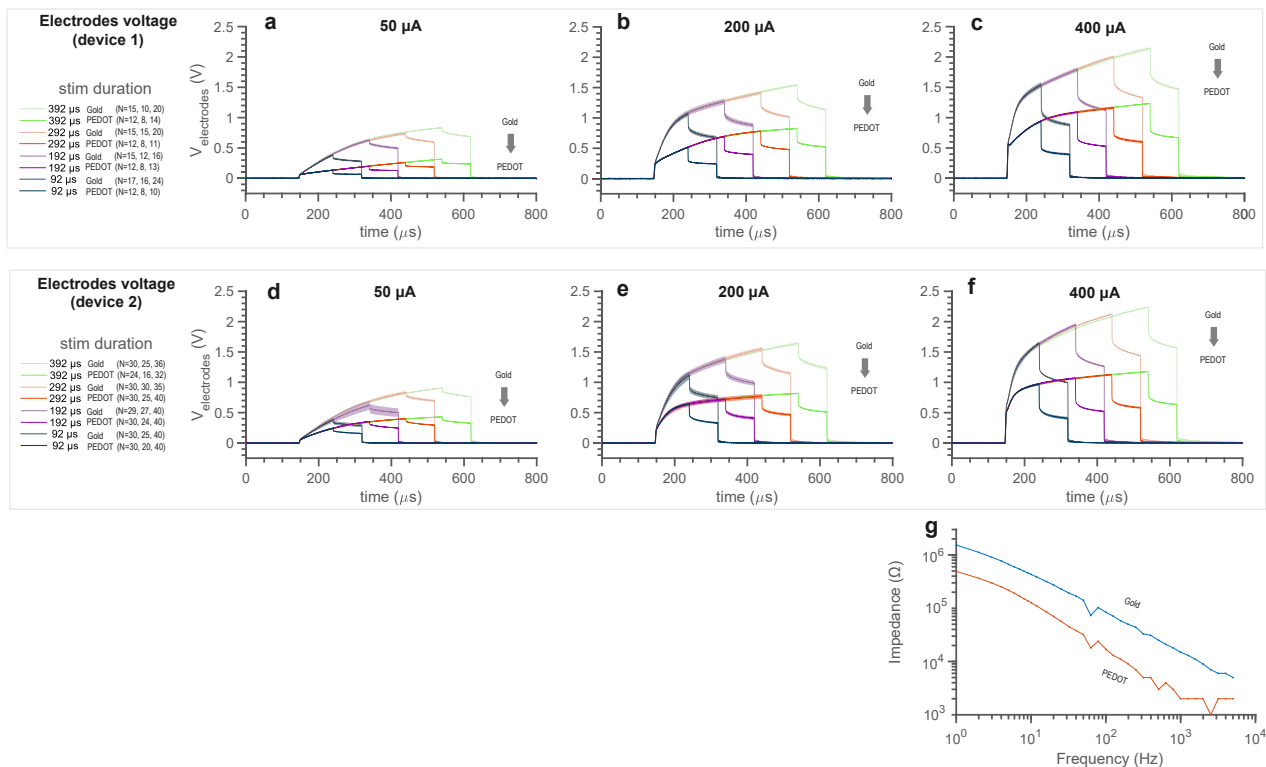


Figure S8 | Stimulation electrodes characterization in saline. a, b, c, d, e, f, The electrode voltage during stimulation pulses was measured for two devices before and after PEDOT:PSS (poly(3,4-ethylenedioxythiophene) polystyrene sulfonate) plating (a third device was tested but is not shown due to a suspected short). Each device that was tested was an inactive mote which had stim electrode and ground testing leads connected to the corresponding testing leads of a functional mote that was acoustically driven and provided the stimulation current pulses. g, Impedance spectrum before and after PEDOT:PSS plating (device 1). (a-f): For each condition, the coloured line represents the trial-average voltage at each point in time, the width of the shaded error region is ± 1 s.d.. N, given on the left, is the number of stim events in each condition in each of the three panels to the right, respectively. A total of 26 pulses out of 1076 are not shown due to shorting region timing glitches. All replications for a given condition are separate stimulation events in a single *in vitro* experimental setup. N = 1 sweep for each condition in data in panel g.

StimDust adopts a design with monophasic stimulation and charge balance via electrode shorting (also known as passive recharge). This enables operation with a single power supply, saving area, power, and complexity on the volume- and power-constrained wireless device. This passive charge-balancing approach has been used successfully in clinical stimulators; Parastarfeizabadi and Kouzani 2017⁶ write: “most of the available market-based open-loop and closed-loop DBS systems use a passive charge-balancing scheme.” The passive charge balance leads to a discharge

current as the remaining charge stored at the electrode interface flows through the tissue solution resistance during the shorting phase. Unlike many monophasic stimulators, StimDust has bipolar electrodes in close proximity and of identical area. As such, there is no asymmetry in current density at the electrodes, as there is for a monopolar stimulator which utilizes, for example, the large surface of an implanted titanium can as the return electrode. To ensure that this charge-balance current does not present any danger to the tissue, the tissue interface was modelled.

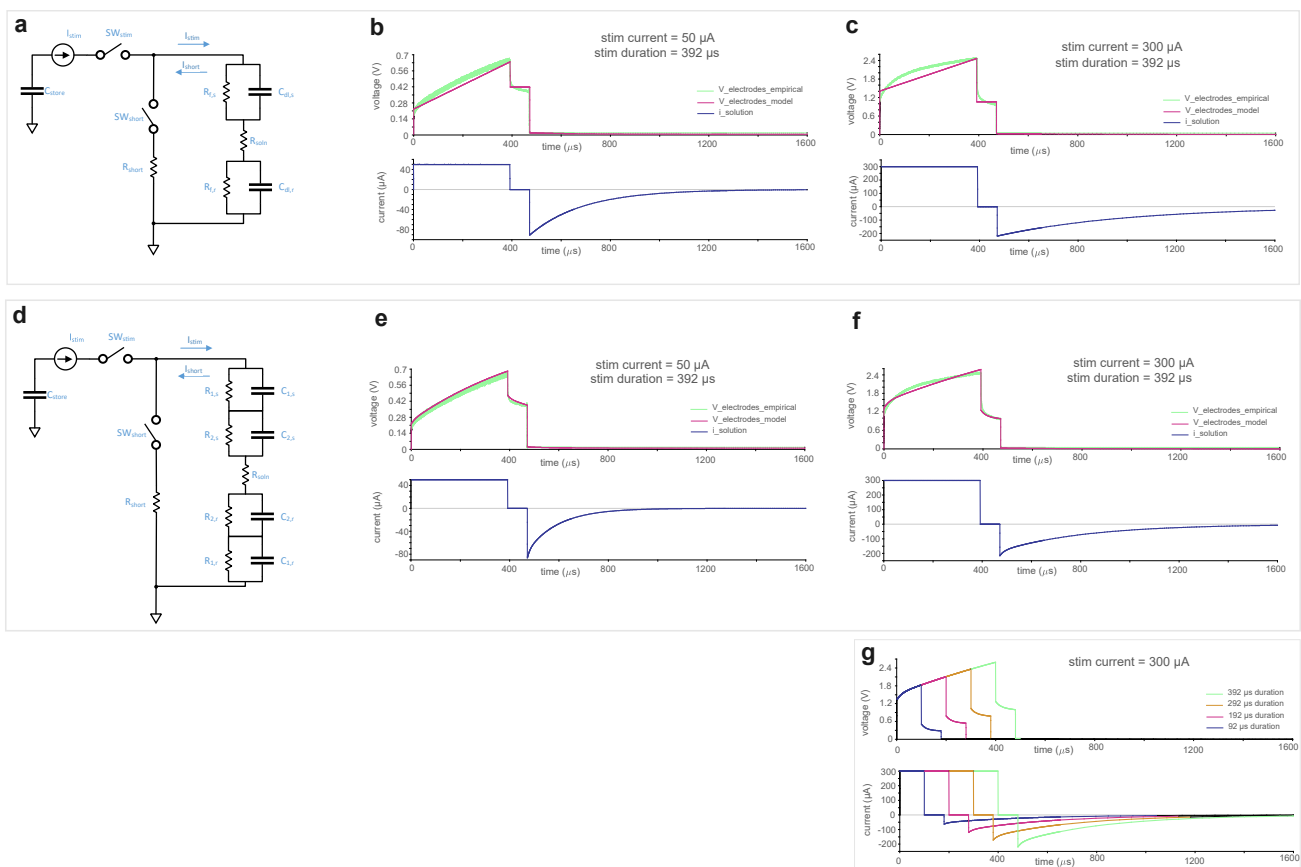


Figure S9 | Monophasic stimulation and charge balancing. **a**, simplified stimulator model (model A) with a simple electrode model: Cdl - Rs - Cdl. $R_{f,s}$ and $R_{f,r}$ are ignored in this model. **b**, 50 μ A, 392 μ s pulse fit to empirical data from animal D (parameters 95 nF, 4.4 kOhm). **c**, 300 μ A, 392 μ s pulse fit to empirical data from animal D (parameters 222 nF, 4.7 k Ω). **d**, simplified stimulator model (model B) with R1||C1 - R2||C2 - Rs - R2||C2 - R1||C1 electrode model. **e**, 50 μ A, 392 μ s pulse fit to empirical data from animal D (parameters 300 Ω , 40 nF, 8.6 k Ω , 65 nF, 4.2 k Ω). **f**, 300 μ A, 392 μ s pulse fit to empirical data from animal D (parameters 350 Ω , 55 nF, 6.0 k Ω , 190 nF, 4.4 k Ω). **g**, sweep of stimulation pulse duration from 100 μ s to 600 μ s (parameters: same as in f).

To model this, two circuits were simulated, each with a pulsed current source, an electrode-tissue equivalent circuit, and a shorting switch with shorting resistance (Fig S8). Stimulation current was applied for the (W) stim width phase; the electrodes were in a high-impedance state for the (G) interphase gap; and the shorting switch was closed for the (S) shorting phase. The resistance along the shorting path in the mote IC (R_{short}) is 130Ω (the on-resistance of the shorting NMOS transistor (n-channel metal oxide semiconductor transistor) in Fig.3b). This reduces the maximum charge balance current and is independent of the tissue solution resistance. In model A, the electrode-tissue equivalent circuit is simplified to just a double-layer capacitance C_{dl} at each electrode, and a solution resistance R_{soln} . This model is not perfect at fitting the shape of the stimulation pulse, but is widely used and easy to analyse. Model B considers a $R1\parallel C1 - R2\parallel C2$ at each electrode, with a solution resistance R_{soln} in between. This equivalent circuit has been shown to fit the behaviour of neural stimulating electrodes⁷. It avoids an explicit constant phase element, as seen in some electrode impedance models which are analysed only in the frequency domain⁸, because these elements take more parameters (RC elements) to model in the time domain⁹.

Initial estimates of parameter values were generated using Zfit¹⁰ on impedance spectroscopy data in PBS. Parameter estimates were then adjusted in a time-domain SPICE model to both peg the simulated electrode voltage at the end of the interphase gap to the empirical data from animal D and to fit the shape of the stimulation voltage as closely as possible. Through this fitting process, there was some variability or uncertainty in capacitor values, but little uncertainty in the series solution resistance. The maximum charge balance current depends almost entirely on the electrode voltage at the end of the interphase gap and the series solution resistance. The former is known empirically and the latter has a confident modelled value. Therefore, the estimates for maximum charge balance current are good. The estimates for the charge balance current time constant are slightly less certain due to lower confidence in the correct modelling of capacitive effects at the electrode interface.

model	parameters	i_{stim} (μA)	Maximum charge balance current (μA)	Maximum charge balance current relative to stim current	Duration that charge balance current is greater than stim current	Time to discharge below 1 mV (μs)
A	100 nF, 4.4k Ω	50	83	167%	116	1344
A	100 nF, 4.4k Ω	100	131	131%	61	1447
A	100 nF, 4.4k Ω	150	162	108%	18	1495
A	100 nF, 4.4k Ω	200	162	81%	0	1495
A	100 nF, 4.4k Ω	250	185	74%	0	1524
A	100 nF, 4.4k Ω	300	211	70%	0	1555
A	100 nF, 4.4k Ω	350	228	65%	0	1572
A	100 nF, 4.4k Ω	400	245	61%	0	1588
A	250 nF, 4.8 k Ω	50	77	153%	263	3657
A	250 nF, 4.8 k Ω	100	131	131%	167	3936
A	250 nF, 4.8 k Ω	150	162	108%	48	4066
A	250 nF, 4.8 k Ω	200	162	81%	0	4068
A	250 nF, 4.8 k Ω	250	185	74%	0	4147
A	250 nF, 4.8 k Ω	300	211	70%	0	4230
A	250 nF, 4.8 k Ω	350	228	65%	0	4278
A	250 nF, 4.8 k Ω	400	245	61%	0	4321
B	300 Ω , 40 nF, 8.6 k Ω , 65 nF, 4.2 k Ω	50	89	179%	52	729
B	300 Ω , 40 nF, 7.6 k Ω , 90 nF, 4.3 k Ω	100	137	137%	28	1068
B	300 Ω , 40 nF, 6.6 k Ω , 110 nF, 4.3 k Ω	150	172	115%	10	1304
B	325 Ω , 55 nF, 6.6 k Ω , 165 nF, 4.3 k Ω	200	174	87%	0	1969
B	330 Ω , 55 nF, 6.3 k Ω , 185 nF, 4.3 k Ω	250	197	79%	0	2230
B	350 Ω , 55 nF, 6.0 k Ω , 190 nF, 4.4 k Ω	300	221	74%	0	2352
B	350 Ω , 55 nF, 6.0 k Ω , 215 nF, 4.4 k Ω	350	236	67%	0	2676
B	350 Ω , 55 nF, 6.0 k Ω , 235 nF, 4.4 k Ω	400	251	63%	0	2957

Table S2 | Charge balance current values from empirically pegged and fit simulations of the stimulation pulse. The first set of simulations with model A use parameters from the range of fit parameters which yield maximal peak charge balance current. The second set of simulations with model A use parameters from the range of fit parameters which yield maximal discharge time.

Simulations were run and the charge balance current was measured, with key values extracted (Table S2). The simulations were performed with a stimulation pulse duration of 392 μs . This was the longest pulse duration utilized by StimDust, and is in the ‘saturation’ region of the recruitment curve by stimulation duration (Fig 8f). Peak charge balance current varies roughly linearly with stimulation pulse duration (Fig S8g), so pulses with duration less than 392 μs will have charge balance current values lower than those reported in Table S2.

Taken together, the data in Table S2 show that peak charge balance current never exceeds 251 μA , well below the nominal maximum stimulation current of 400 μA . Furthermore, the amount of time before charge balance current falls below the nominal stimulation current is substantially less than the stimulation pulse duration. All of these values would be less for shorter pulse durations. Importantly, most literature reporting the threshold for tissue damage is closely linked to charge

per phase and charge density per phase¹¹. The total charge transferred during the charge-balance phase is necessarily less than or equal to that during the stimulation phase. Stimulation protocols used in this work are plotted against the Shannon equation in Figure S9.

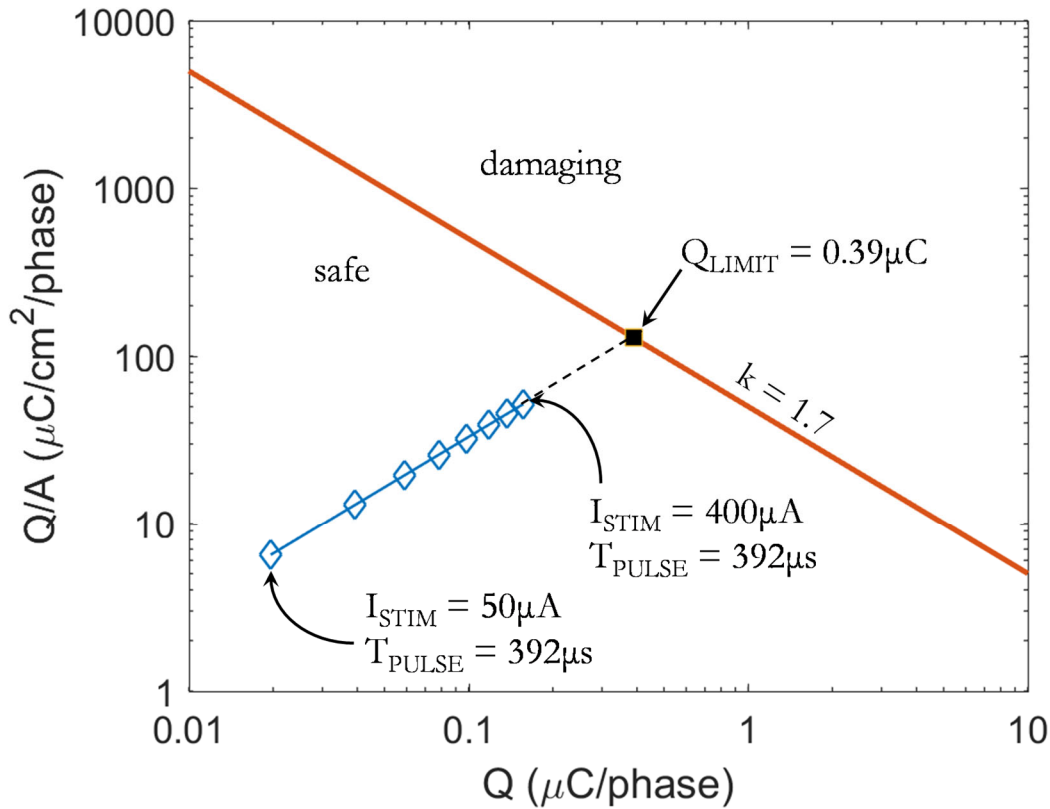


Figure S10 | Charge (Q) vs. charge density (Q/A) for safe stimulation limits. (Using $k = 1.7$). Data below the $k = 1.7$ line predict safe operation. The largest stimulation pulse used in this work is 40% of the limit. T_{PULSE} is stimulation pulse duration.

The Shannon equation incorporates pulse width, current, and electrode area, but does not directly account for short, high intensity current pulses which can accompany passive recharge. Butterwick et. al. 2007 mapped the strength-duration dependence of damage thresholds for retinal cells. Assuming a damage threshold of $1 \text{ mA}/\text{cm}^2$, we estimated R_{soln} for square electrodes *in vivo* and in saline for various areas to determine the charge balance current density ($J_{\text{charge_balance}}$). We assumed a bipolar, symmetric electrode configuration and that the maximum stored electrode voltage was 1.2V (Figure S10).

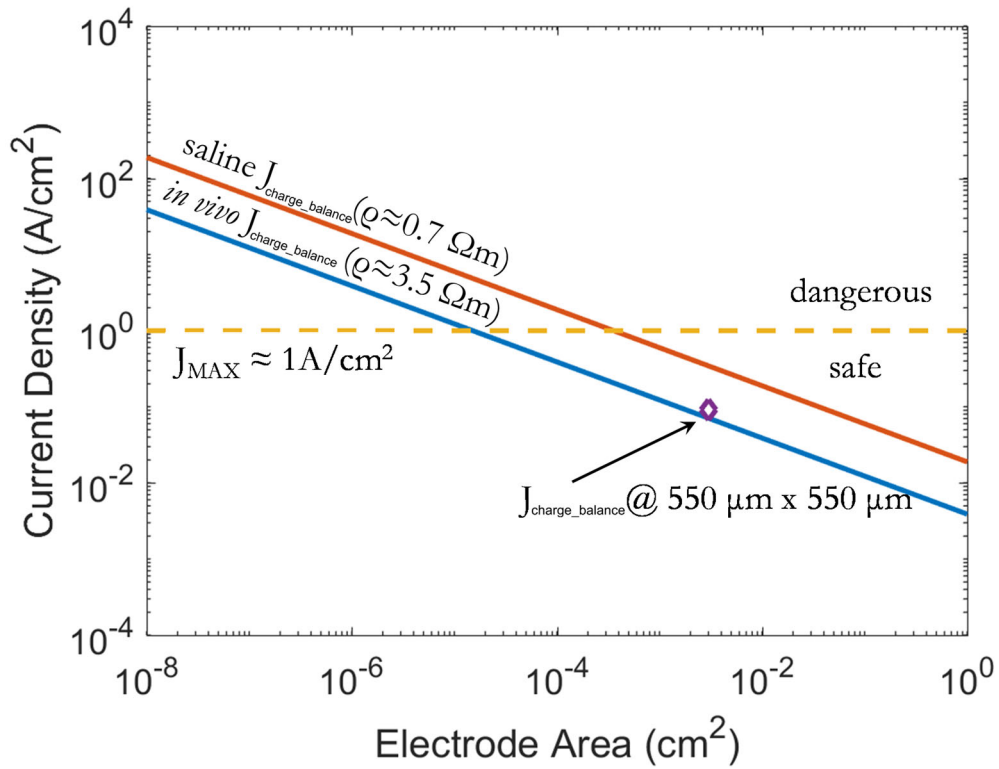
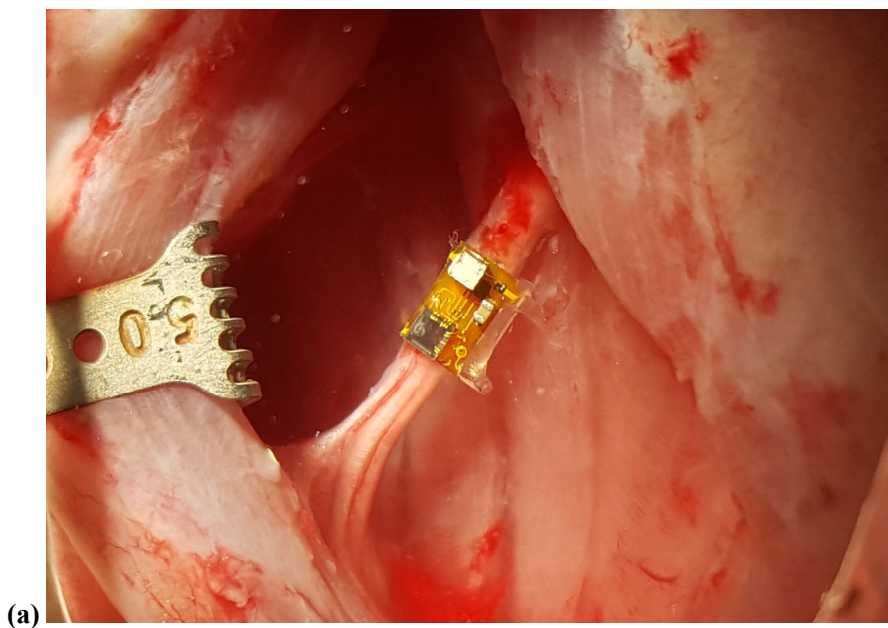
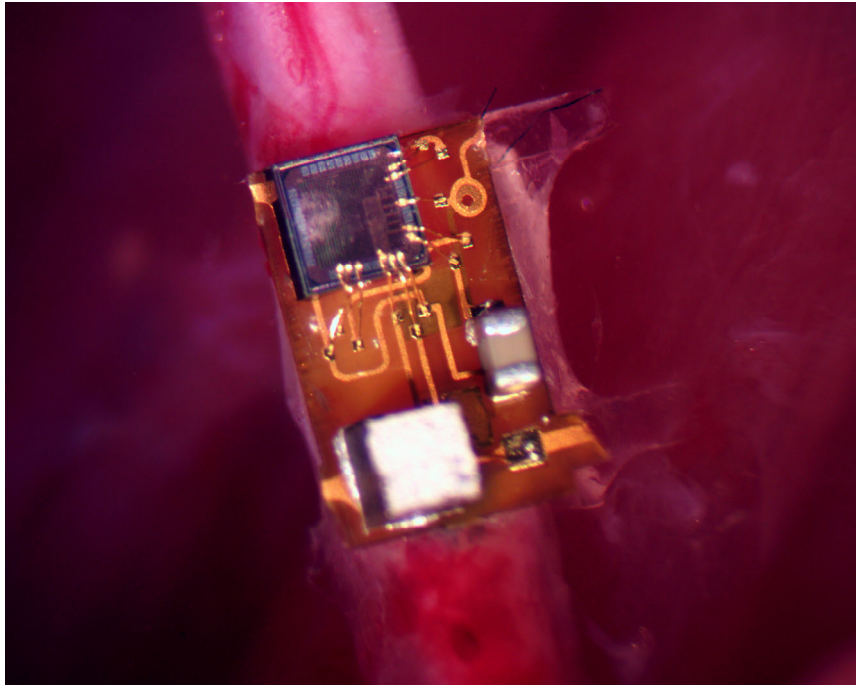


Figure S11 | Charge balance current density vs. square electrode area in saline and *in vivo*.

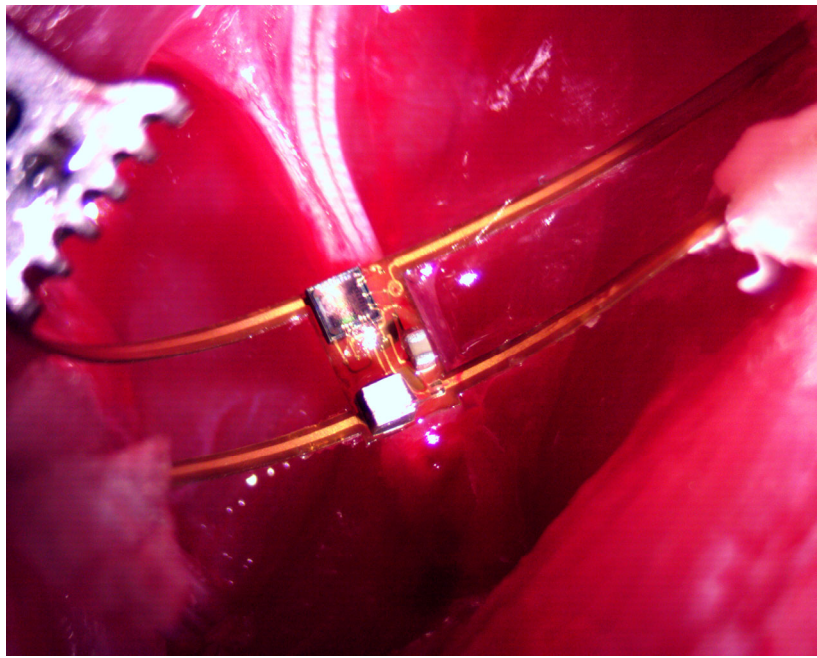
As the stimulation and return electrodes scale to smaller, the discharge current can exceed the $1 A/cm^2$ damage threshold. The diamond represents the maximum discharge current for this work.

Supplementary Section 5: Additional photographs





(b)



(c)



(d)

Figure S12 | Alternate images for Fig 1b, Fig 1c, and Fig 1d.
See main text Figure 1 caption for descriptions.

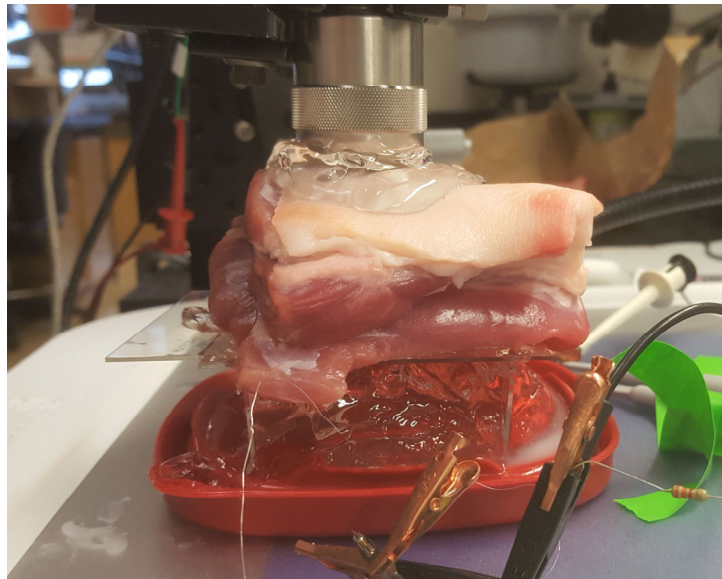


Figure S13 | Alternate image for Fig 4c taken from a different angle.
See main text Figure 4 for description.

References

1. Azhari, H. Appendix A: Typical Acoustic Properties of Tissues. *Basics Biomed. Ultrasound Eng.* 313–314 (2010). doi:10.1002/9780470561478.app1
2. Jiménez, N. *et al.* Nonlinear Acoustics FDTD method including Frequency Power Law Attenuation for Soft Tissue Modeling. *arXiv* (2014).
3. Nassiri, D. K., Nicholas, D. & Hill, C. R. Attenuation of ultrasound in skeletal muscle. *Ultrasonics* **17**, 230–232 (1979).
4. Ye, P. P., Brown, J. R. & Pauly, K. B. Frequency dependence of ultrasound neurostimulation in the mouse brain. *Ultrasound Med. Biol.* **42**, 1512–1530 (2016).
5. Downs, M. E. *et al.* Non-invasive peripheral nerve stimulation via focused ultrasound *in vivo*. *Phys. Med. Biol.* (2017). doi:10.1088/1361-6560/aa9fc2
6. Parastarfeizabadi, M. & Kouzani, A. Z. Advances in closed-loop deep brain stimulation devices. *J. Neuroeng. Rehabil.* **14**, 79 (2017).
7. Montero-Rodriguez, J. J., Schroeder, D., Krautschneider, W. & Starbird, R. Equivalent circuit models for electrochemical impedance spectroscopy of PEDOT-coated electrodes. *IEEE Ger. Student Conf.* (2015).
8. Abidian, M. R. & Martin, D. C. Experimental and theoretical characterization of implantable neural microelectrodes modified with conducting polymer nanotubes. *Biomaterials* **29**, 1273–1283 (2008).
9. Valsa, J. & Vlach, J. RC models of a constant phase element. *Int. J. Circuit Theory Appl.* **2**, n/a-n/a (2011).
10. Dellis, J.-L. Zfit. *Matlab Mathworks File Exchange* (2010). Available at: <https://www.mathworks.com/matlabcentral/fileexchange/19460-zfit>.
11. Shannon, R. V. A model of safe levels for electrical stimulation. *IEEE Trans. Biomed. Eng.* **39**, 424–426 (1992).